

Scanning eye-safe depolarization lidar at 1.54 microns and potential usefulness in bioaerosol plume detection

Shane D. Mayor, Scott M. Spuler, and Bruce M. Morley

National Center for Atmospheric Research, Boulder, Colorado, USA

ABSTRACT

Effective monitoring of the atmosphere for potentially hazardous aerosol plumes in urban areas requires a lidar that produces high signal-to-noise backscatter returns, fine spatial resolution, rapid updates, eye-safety at all ranges, and long-range operation. A scanning elastic backscatter lidar with high pulse energy that meets these requirements was recently developed at NCAR. The latest upgrades to the lidar system include the use of a new Raman cell for wavelength conversion and a two-channel receiver for backscatter depolarization ratio measurements. Highlights from recent field tests of the system are presented and plans to improve the prototype, as well as construct an unattended and continuously operating version, are discussed.

Keywords: lidar, aerosol, bioaerosol, polarization, biological terrorism

1. MOTIVATION

The present threat of aerosol bioterrorism requires us to consider deployment of technologies that are available today. Ideally, the solution to the problem of quickly detecting a deliberately released pathogenic aerosol cloud in an urban area would be provided by a remote sensor that could discriminate a lethal cloud from common aerosol plumes and act as an alarm. Unfortunately, this is an especially difficult technical challenge for active systems when one adds the practical requirements of eye-safe, continuous and long-range operation. The problem is further confounded by the wide variety of pathogens a terrorist could release and their varying optical properties.¹

A biological attack in a city could target a specific high profile building or be released with the intent of infecting a broad region. In both of these scenarios, the non-discriminating elastic backscatter lidar may be able to play a defensive role. In the case of protecting a specific high profile building, an elastic backscatter lidar could be used to monitor all approaching plumes and close the building's ventilation until the aerosol type is determined by in situ sensors.² In the case of protecting a large urban region, networks of elastic backscatter lidars could operate in a surveillance mode continuously recording and archiving the distribution of all significant aerosol emissions and their advection and diffusion. These data would be used as a form of intelligence after an attack was detected by in situ sensors or epidemiological indicators. In this case, it is hoped that the aerosol plume responsible for the outbreak could be observed in the archived data thereby allowing authorities, investigators, and emergency response crews to focus on drug distribution and interdiction to prevent additional attacks. If the offensive plume is not recognizable in the archive, the observational history of the microscale flow structure as revealed by the background aerosol should be useful to determine the trajectories or dispersion patterns during the period of concern. This concept of operations was recently proposed by Dr. Richard Danzig in his keynote address to the American Meteorological Society's Second Symposium on Lidar Atmospheric Applications and summarized in a forthcoming article.³

The urban atmospheric boundary layer is filled with a variety of aerosol plumes from everyday activities plus spatial variability of aerosol concentration due to turbulence. This makes the problem of plume detection and tracking even more challenging. Therefore, it would be useful to the above hazardous plume detection problem if an elastic backscatter lidar had some type of ability to delineate aerosol plumes of interest from the background aerosol distribution. Toward this, we have recently added a backscatter depolarization capability on the elastic lidar that is described in the following pages. We also present highlights of test results with controlled aerosol releases at Dugway Proving Ground. This paper is the first documentation of these very recent results.

Corresponding author: Dr. Shane D. Mayor, E-mail: shane@ucar.edu, Telephone: 303 497 2037

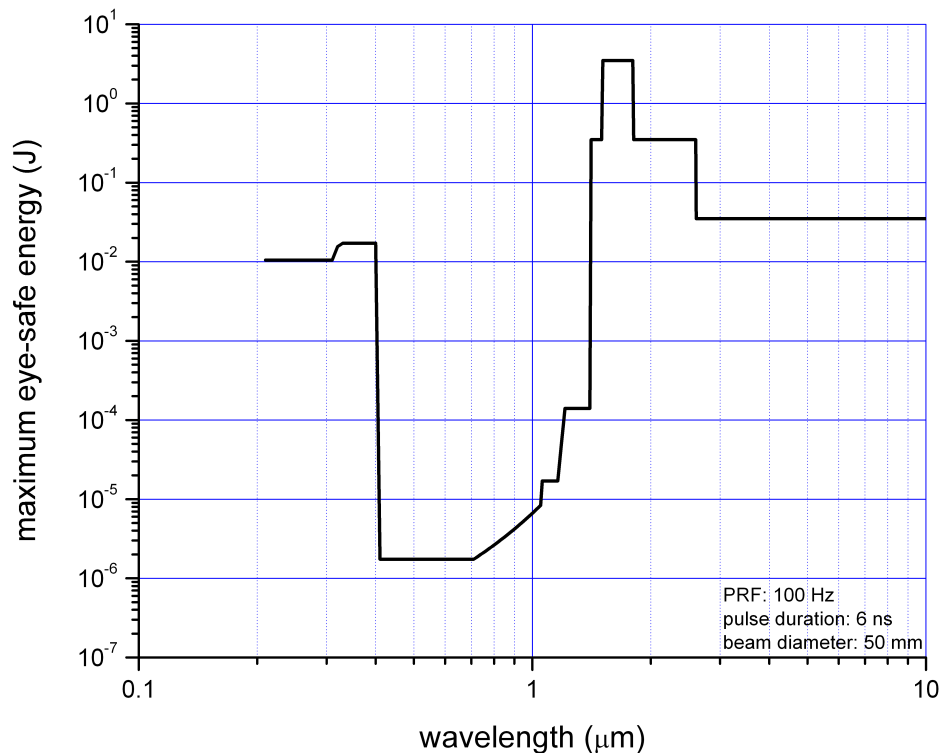


Figure 1. Maximum eye-safe laser energy as a function of wavelength for a pulse repetition frequency of 100 Hz, pulse duration of 6 ns, and beam diameter of 50 mm.

2. DESCRIPTION OF THE SENSOR

NCAR's Raman-shifted Eye-safe Aerosol Lidar (REAL) was designed to be an atmospheric research instrument—capable of rapidly revealing the structure of the clear atmosphere. Eye-safety is imperative for today's research lidars, especially in urban environments. Furthermore, the lidar should be powerful and sensitive so that it can detect variability in the background aerosol quickly with a high signal-to-noise ratio. Lidar systems often add (or average) backscatter return from several laser pulses to obtain greater signal-to-noise ratio. However, this approach suffers from the additional receiver noise associated with each pulse. The alternative approach used in REAL is to transmit sufficiently high pulse energy for long range detection in a single shot.

To achieve this goal, we chose to operate at a wavelength that lies within a band that is the safest in the entire optical spectrum. Photons in the 1.5 to 1.8 micron band are absorbed over several millimeters of depth in the aqueous humour of the eye. At visible and shorter IR wavelengths, photons can reach the retina causing damage. At longer wavelengths, and in the UV, they are absorbed near the eye's surface potentially damaging the cornea. The American National Standard for Safe Use of lasers (ANSI 2000) reports that this band is the highest allowable eye-safe region, as shown in Fig. 1. The pulse energy which can safely be transmitted is approximately one and two orders of magnitude higher than 2.0 and 10 micron Doppler lidar systems, respectively. For example, fig. 1 (computed using a pulse repetition frequency of 100 Hz, a pulse duration of 6 ns, and a beam diameter of 50 mm) shows that it is possible to safely transmit over 2 J per pulse at 1.5 microns. REAL presently operates with pulse energies one order of magnitude lower than this.

The first generation REAL (a prototype system denoted "REAL v1") was developed at NCAR over the past several years.^{4,5} The transmitter begins with a flash-lamp pumped, Nd:YAG laser capable of generating 800

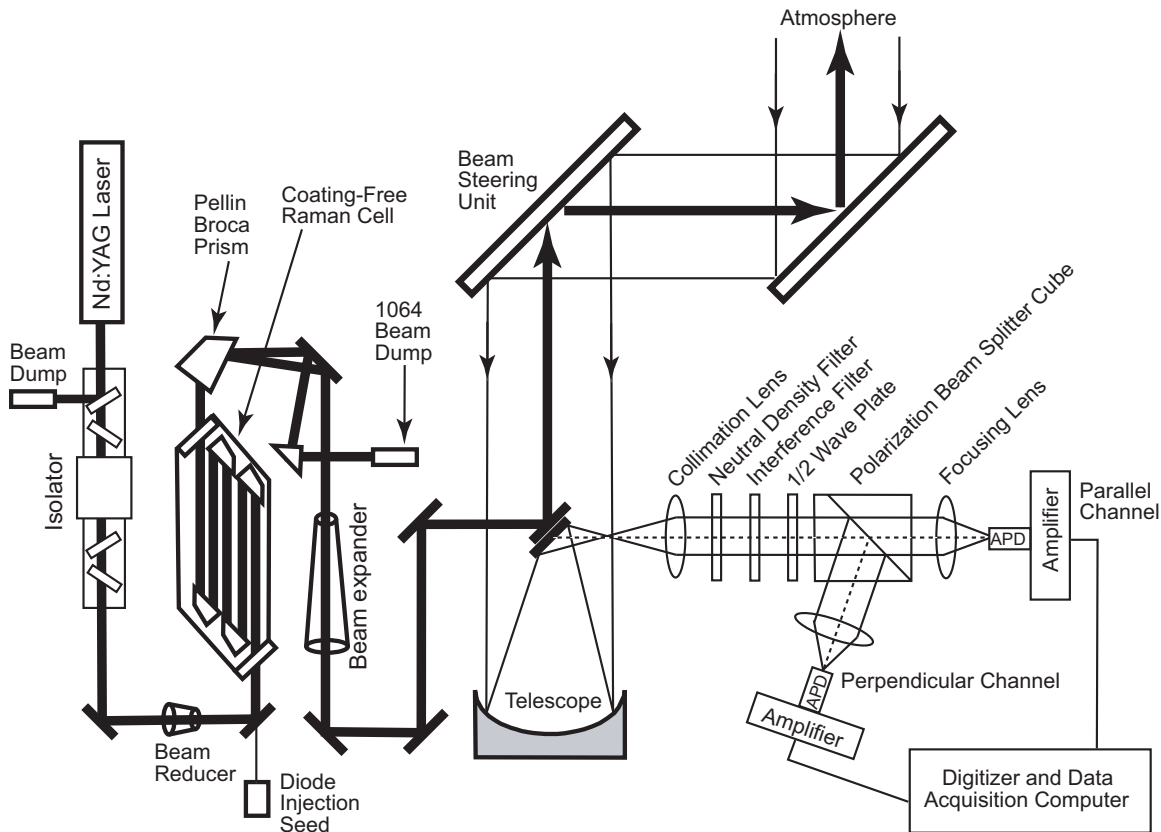


Figure 2. System schematic of the Raman-shifted Eye-safe Aerosol Lidar (REAL) using the coating-free Raman cell and the two-channel depolarization receiver.

mJ/pulse energy at 1064 nm wavelength (Continuum Surelite III). The pump operates with a pulse repetition frequency (PRF) of 10 Hz. The pump beam is converted to the eye-safe wavelength via stimulated Raman scattering (SRS) in a high pressure cell filled with methane. The frequency converter is designed to overcome the historical limitations of methane active SRS technology. Light exiting the Raman cell enters a high dispersion prism, physically separating the residual pump beam from the 1.5 micron Stokes beam. The 1.0 micron beam is safely blocked and the 1.5 micron beam is expanded and transmitted into the atmosphere by an azimuth-over-elevation beam steering unit (BSU). Photons elastically backscattered from aerosol particles are directed by the BSU mirrors and collected with a 40 cm diameter Newtonian telescope. The backscattered light is collimated to facilitate transmission through a subsequent bandpass interference filter and focused, with a custom low f-number lens set, onto a photodiode. The receiver allows containment of a 0.56 mrad field-of-view on the detector. A schematic of the current system is shown in Figure 2.

Solid-state wavelength converters in the 1.5 micron region do exist,⁶ however one that is capable of generating the requisite high pulse energy and low beam divergence necessary for a direct-detection lidar has not been found. Beam divergence is critically important because a lidar's transmitted beam must have a divergence less than the angle corresponding to the receiver's field-of-view in order to achieve full overlap. Currently, it is most practical to use InGaAs avalanche photodiodes (APD) as detectors for lidars at this wavelength. The maximum active area of this type of detector is 200 microns in diameter. This small detector therefore subtends a very narrow field of view and places a requirement of low divergence on the transmit beam.

Historically, the use of Raman cells to reach 1.5 microns had severe limitations. High energy lasers were focused inside pressurized cells to reach the energy density required for efficient SRS conversion. The high energy density from these "focused-geometry" cells leads to dissociation of the methane gas, producing carbon

soot which coated the optical elements. Another problem with previous methane Raman shifters is the local heating effect. During the conversion process, the energy difference between the pump and SRS photons is deposited into the gas as heat. Since the gas index of refraction is a function of temperature this leads to defocusing and poor beam quality.

Within the last three years, NCAR has designed, constructed and operated two new generations of Raman cells that overcome these traditional problems. In our approach, dissociation of the methane gas is entirely eliminated by not focusing the pump beam in the cell. High conversion efficiency is maintained by increasing the path length through the cell with a folded path geometry. The long path length also improves beam quality because the heating is distributed over a larger volume thereby reducing temperature gradients along the beam. Lastly, these Raman cells circulate the methane in order to move the heated gas out of the beam path prior to the next shot.

The first generation Raman cell (see Fig. 3a) employs entrance and exit windows, and internal mirrors, that are within a few degrees of perpendicular to the beam. Despite the great improvement over traditional cells, this design still had some disadvantages. First, the windows required anti-reflection (AR) coating to prevent losses each the time beam passes through. Second, the internal mirrors are parallel and therefore the beam path is slightly overlapped with itself in front of each mirror. These doubly illuminated volumes can potentially degrade the beam quality. The AR and high reflection (HR) coatings can be problematic for two reasons. First, unavoidable manufacturing defects in the coatings can result in burning of the coating in the presence of a high energy laser beam. Second, even with a good coating, slow photochemical etching occurs on the interior sides of the windows due to the interaction of the coating material with the methane in the presence of the intense IR light. This effect is very slow, but it was sufficient that we replaced the windows with uncoated substrates on one side (the interior side) within a year.

Without injection seeding the Raman cell, the Stokes field is initiated by spontaneously emitted photons. This stochastic process causes the energy and spatial characteristics of the output beam to fluctuate. The REAL design uses a telecommunications c-band laser to initiate the Stokes field. The result is improved conversion efficiency and beam quality. As mentioned previously, the beam quality is required to reduce the transmission divergence angle below that of the receiver's field of view.

3. RECENT HARDWARE UPGRADES

3.1. Frequency converter

A second generation Raman cell (see Fig. 3b) that eliminates the problems of the first generation cell and provides better performance was designed, fabricated and tested. The second generation cell employs all uncoated optics with surfaces at the Brewster angle. In this design prisms are used to fold the beam within the cell. In addition to eliminating the vulnerable AR and HR coatings, this design eliminates the beam overlap regions. The second generation cell also includes improved internal shrouding and flow straighteners so the gas flows transverse to the beam plane while suppressing turbulence. In addition to the increased optical damage threshold, the cell is essentially lossless when pumped with linearly polarized light. Initial tests of this design indicate that it is capable of high conversion efficiency (>36%). Pumping with 615 mJ/pulse at 10 Hz results in 1.5-micron pulse energies in excess of 225 mJ with good beam quality (M-squared less than 8). The cell is operated with a mixture of 9.5 and 2.7 atm of methane and argon, respectively.

3.2. Polarization

Depolarization measurements with lidar systems are well known and have been used to identify particle shapes or phases of water in clouds over the past 30 years.⁷ For example, it has been demonstrated that spherical particles (i.e. droplets) backscatter linearly polarized laser light in the same polarization plane.^{8,9} As a particle's shape deviates from spherical, some of the incident light is backscattered in other polarization planes. For example, crystals are highly depolarizing. Therefore, by examining the depolarization of a condensed water cloud, one may be able to infer its phase (i.e. liquid or ice).

The initial goal of the work presented here is relative depolarization measurements to assist in the standoff identification and tracking of plumes of interest. Obtaining absolute depolarization with a scanning device, like

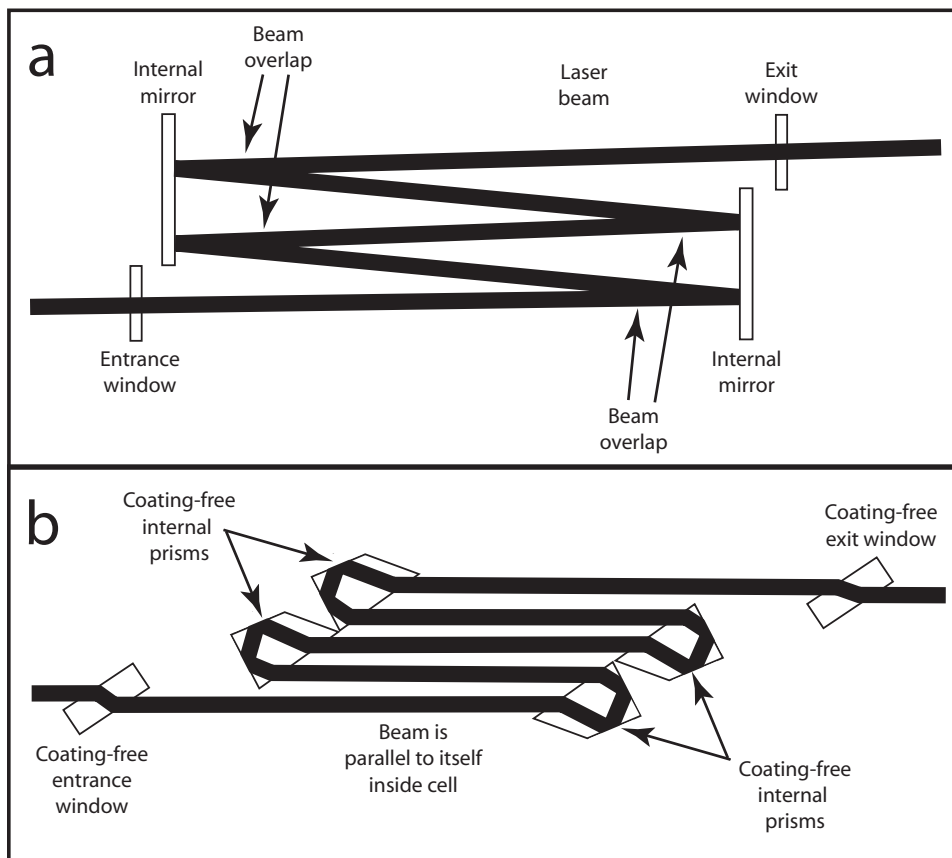


Figure 3. Laser beam path through two generations of Raman cells. a) The first generation used windows and mirrors with anti-reflection and high-reflection coatings, respectively. b) The second generation uses optics with surfaces at the Brewster angle and prisms for total internal reflections. Therefore, no coatings are necessary.

REAL, takes special precautions.¹⁰ Reflection by the scanning mirrors has the effect of rotating the polarization vector of the outgoing laser pulse. Upon propagation back to the receiver, the polarization vector is counter-rotated by the same amount. However, if the aerosols have a preferred orientation, or the mirrors have different reflection coefficients, the absolute measured depolarization will be erroneous. In addition, mirrors impart a small phase difference between the reflected electric field components. This phase difference transforms linear polarization to elliptical which is not restored back to linear by back-propagation. These angle-dependent errors can be minimized with careful attention to the mirror coatings. Currently, protected gold coatings are used on the BSU mirrors. These metallic coatings are inexpensive and considered insensitive to polarization, at least to a first order. The above issue must be addressed to make absolute depolarization measurements.

To implement backscatter depolarization capability on REAL, the polarization purity of the transmit beam was improved by placing an optical isolator at the exit of the Nd:YAG laser. The optical isolator consists of a Faraday rotator and two polarizers (each polarizer is a pair of double dielectric Brewsters plates each with an extinction ratio of 10^{-4} .) This reduces the pump energy entering the Raman cell by about 20 percent to about 615 mJ per pulse. In addition to improving the polarization purity, the isolator protects the pump laser from potential optical feedback. The improved polarization purity is also required for efficient use of the second generation Raman cell which employs six optical elements at the Brewster angle. The polarization purity of the beam transmitted to the atmosphere is well in excess of 10000:1.

Figure 4 shows a ray trace of the receiver from the focal plane of the telescope to the two photodetectors. This portion of the instrument is completely contained within a 30 x 35 x 19 cm enclosure to shield it from any scattered light of the nearby transmitter. The first element of this assembly is a focusing lens designed to

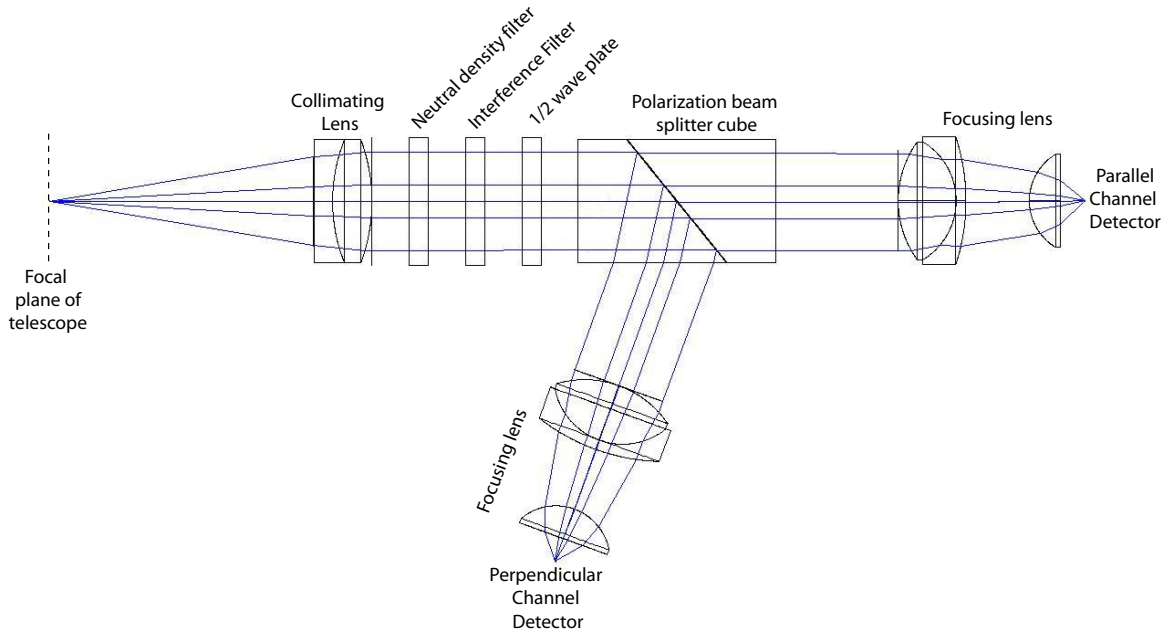


Figure 4. Ray trace of the receiver from the focal plane of the telescope to the two detectors.

collimate the light for transmission through several subsequent optics. These include a neutral density filter, an interference filter, a 1/2 wave plate, and a calcite air-gap Glan Taylor polarization beam splitter cube. The neutral density filter is part of a filter wheel that allows the backscatter signal to be attenuated to prevent saturation and reduce the risk of damaging the photodetectors from hard target reflections. The filter wheel has 6 settings: 0, 0.5, 1.0, 1.5, 2.0, and 2.5. These correspond to transmissions of 100, 31.6, 10.0, 3.16, 1.0, and 0.316 percent, respectively.

The polarization beam splitter cube has a 25 mm clear aperture. Backscattered light returned from the atmosphere in the same polarization plane that was transmitted passes through the cube and is focused on the InGaAs APD on the right side of the diagram (referred to as the parallel channel). The orthogonal polarization state of the backscattered light is reflected out the side of the polarization beam splitter cube at an angle of 109.9 degrees relative to the axis of the parallel beam. This light is focused on to a second InGaAs APD at the center and bottom of the diagram (referred to as the perpendicular channel). The beamsplitter cube has an extinction ratio of 10^{-6} for the transmitted beam. The reflected beam (the perpendicular channel) contains 3% of the parallel polarized light, however it is reflected at a slightly different angle exiting the cube. This difference in angles is sufficiently large given the fast focusing lens and small detector diameter that most (99.7%) of those rays miss the active area. The resulting effective extinction ratio in this channel is 10^{-4} .

The 1/2 wave plate is installed in a rotary mount in order to rotate the backscattered light and line it up with the axis of the polarization beam splitter. In addition, during setup the wave plate is oriented to split the signal equally allowing adjustment of the detector amplifier gains until they match.

3.3. Receiver electronics

Several improvements were made to the detector/amplifier modules as described in Spuler and Mayor.⁵ We use Perkin-Elmer C30659-1550-R2A InGaAs APDs. This off-the-shelf component features a photodiode and preamplifier in a single device. The diameter of the active element is 200 microns and the bandwidth of the entire device is 50 MHz. The module provides the ability of adjusting the bias of the photodiode to compensate for changes in temperature. This capability was added for the field tests described in the next section. Photodiode bias stabilization is performed by Labview software that reads a voltage from a temperature-sensing diode contained in the package. The Labview program computes a running 10 s mean of the temperature and adjusts the bias of the detector according to a temperature versus gain function described in the manufacturer's specifications.

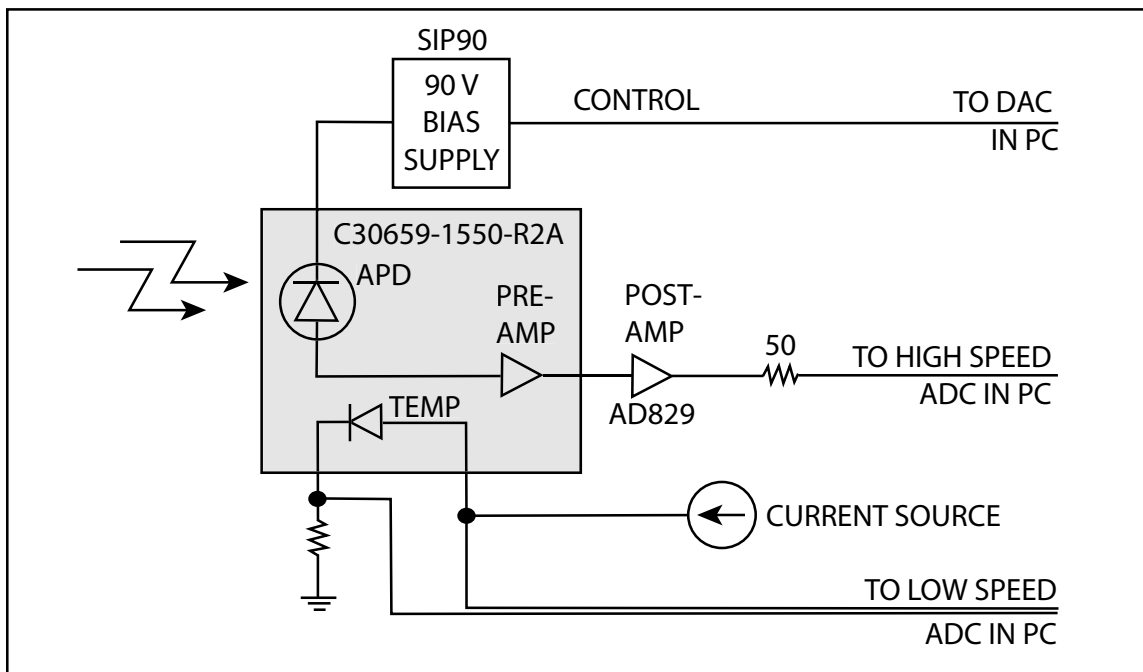


Figure 5. Simplified electronics schematic of the detector/amplifier modules used for the data presented in this paper.

The above detector/preamp module is mounted on a custom electronics board with a post amplifier stage in order to (1) provide additional gain, (2) provide adjustability of the voltage offset to fall within the input range of the digitizer, (3) drive a 50 ohm coaxial cable (to allow a large distance between the amplifier and data acquisition computer), and (4) provide adjustable gain so that the equivalent amount of optical power from the two modules have identical signal levels on the data acquisition system. The post amplifier is an AD829 op-amp operating in an inverting configuration. The bandwidth of the post amplifier stage is between 70 and 75 MHz depending on the gain setting. Figure 5 shows the general layout of this configuration.

4. RESULTS

The system described above, with the second generation Raman cell and depolarization receiver, was deployed at the U.S. Army's Dugway Proving Ground, in June of 2005. The purpose of the deployment was to test the system's ability to detect and discriminate biological aerosol clouds. In addition to REAL, several active and passive sensors were under test. Tests for the active sensors were conducted generally in one of three arrangements. First, the lidars were operated in a staring mode where the beams were held stationary while directed lengthwise through a low velocity wind tunnel. Aerosol generators released particles into the tunnel while in situ sensors inside the tunnel measured particle concentration. Second, the lidars were operated in a horizontal staring mode on a test range where the plumes advected across the beams. Third, the lidars scanned horizontally across plumes on the test range. Releases of biological aerosol simulants and other particulate plumes were conducted at night to avoid the rapid dispersion caused by more turbulent daytime boundary layers. Here we present only cases from scanning on the test range.

For each case presented in this section, we show an image of the total backscatter intensity on the left and the backscatter depolarization ratio on the right. Backscatter profiles from each laser pulse are treated independently. The total backscatter intensity is obtained by the following steps. First, the raw signals from the parallel and perpendicular channel are added together at each range gate to form an array called total raw signal. Next, the intensity of the background light is computed by averaging a number of the pre-trigger gates of the total raw signal. This optical background level, a constant for a given return, is subtracted from each

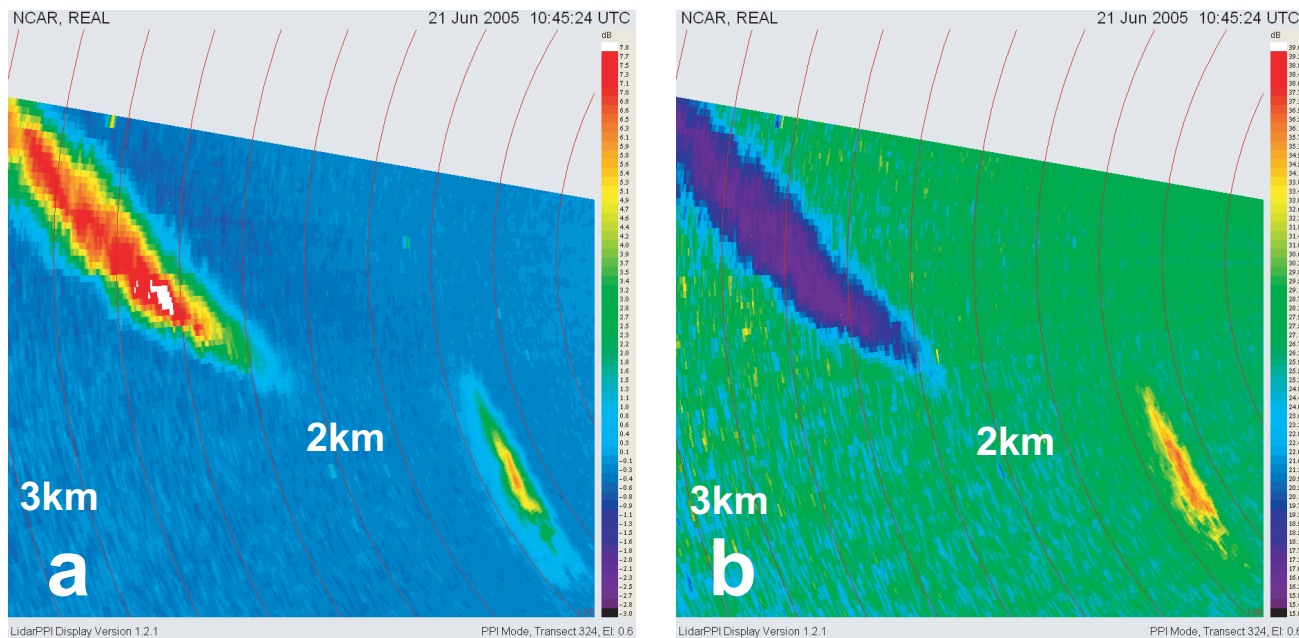


Figure 6. (a) Total backscatter intensity (b) Depolarization ratio. 21 June 2005, 10:45 UTC (4:45 LT). The plume between 2 and 3 km range is “white smoke” from a point release and the plume at 1.5 km range is road dust. In this case, white smoke had a lower depolarization while the road dust had a higher depolarization than the background aerosol ($\sim 11\%$ lower and $\sim 8\%$ higher, respectively.)

element of the total raw signal. This is called the background-subtracted total raw signal. Next, the background-subtracted total raw signal is normalized for shot to shot variations in the amount of laser pulse energy that was transmitted. This is done by computing a factor that rises slightly above unity when the pulse energy falls below a temporal median. The same factor falls slightly below unity when the pulse energy rises above a temporal median. All elements of the background-subtracted total raw signal are multiplied by this energy normalization factor. Next, we multiply each element of the array by the range of the element squared. This removes the one over range-squared dependence in the signal to provide relative aerosol scattering at all ranges. The signal is then converted to decibels (10 times the log of the signal.) Finally, a rolling high pass median filter is applied to remove the effects of low frequency noise, extinction, and shadows. The filter length was set to 1.2 km for all the cases presented here. In this application of REAL, we are most interested in detecting a plume and knowing its location and type. The high pass median filter preserves such small scale features while eliminating the large scale variability. The large scale variability is caused by changes in the background aerosol concentration, extinction, and instrument noise. The backscatter depolarization ratio is computed by dividing the perpendicular channel raw signal by the parallel channel raw signal. For all of the data presented here, the neutral density filter was set to zero to allow 100% transmission.

5. CONCLUSIONS

The images presented demonstrate that it is possible to detect the depolarization caused by some aerosol types. This capability may be useful in identifying and tracking plumes of interest. The first case (fig. 6) in particular confirms that the depolarization ratio varies according to aerosol type and not some other variable such as concentration or range. This case shows a more distant aerosol cloud with substantially lower depolarization than the background aerosol while a closer cloud exhibits higher depolarization. Instrumental systematic errors could not cause this result.

Figure 8 demonstrates that the instrument is capable of measuring the depolarization of aerosol plumes at ranges beyond 7 km. We note that the maximum concentration of the biological plume in this case did not exceed 1500 particles per liter as estimated by an independent method. We note that in a few cases (fig. 10 for example)

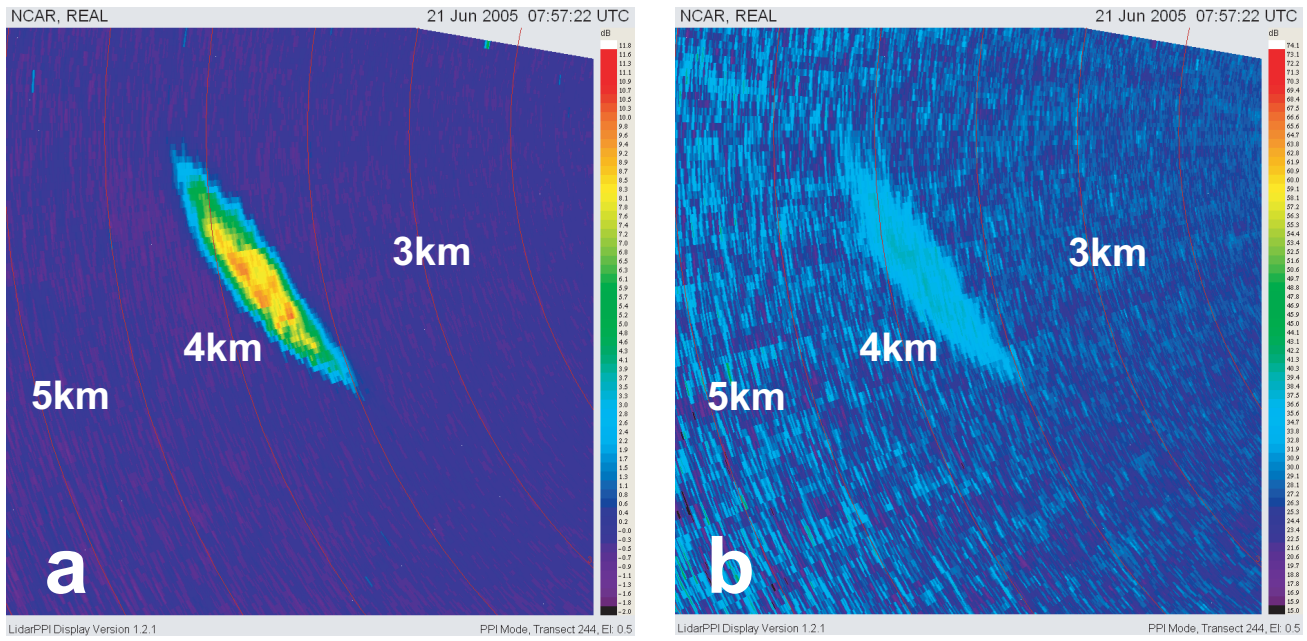


Figure 7. (a) Total backscatter intensity (b) Depolarization ratio. 21 June 2005, 7:57 UTC (1:57 LT). A plume of *Bacillus subtilis* var. *niger* (BG) released from an aircraft at 3.5 km range. In this case, the plume had a higher depolarization than the average of the background aerosol (~8% higher.)

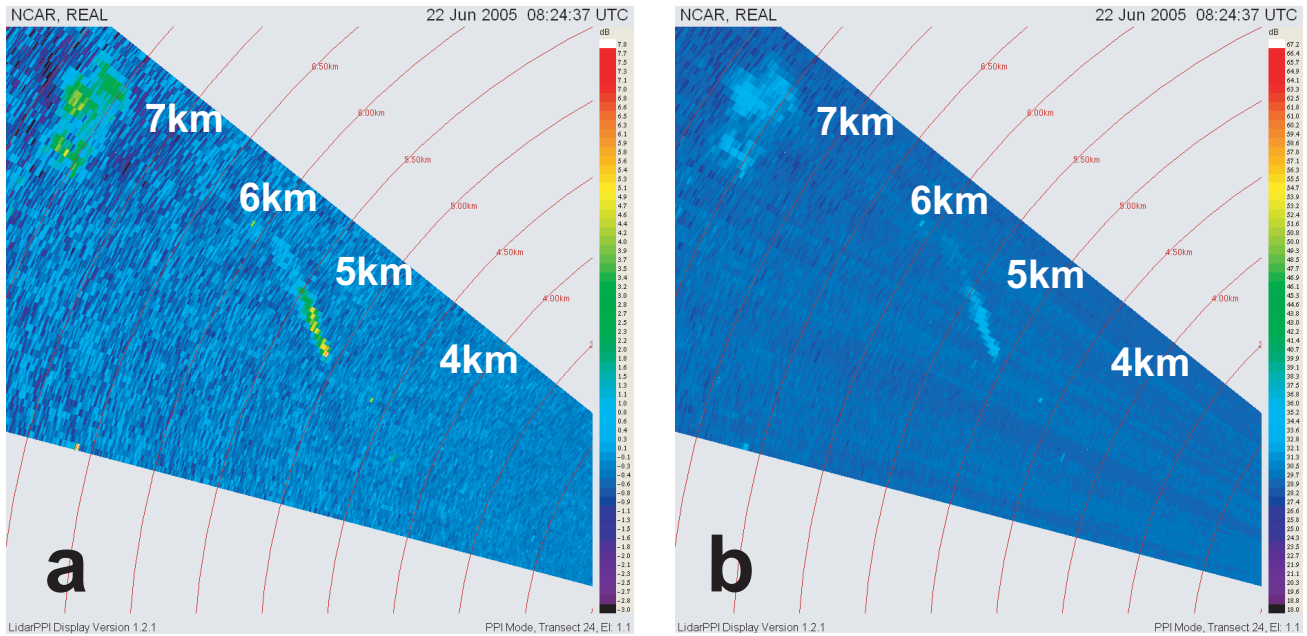


Figure 8. (a) Total backscatter intensity (b) Depolarization ratio. 22 June 2005, 8:24 UTC (2:24 LT). The plume between 5 and 6 km range is a gamma-killed vaccine strain of *Yersinia pestis* (YP) and the plume between 7.4 and 7.9 km is road dust. Both clouds have higher depolarization ratios than the background aerosol.

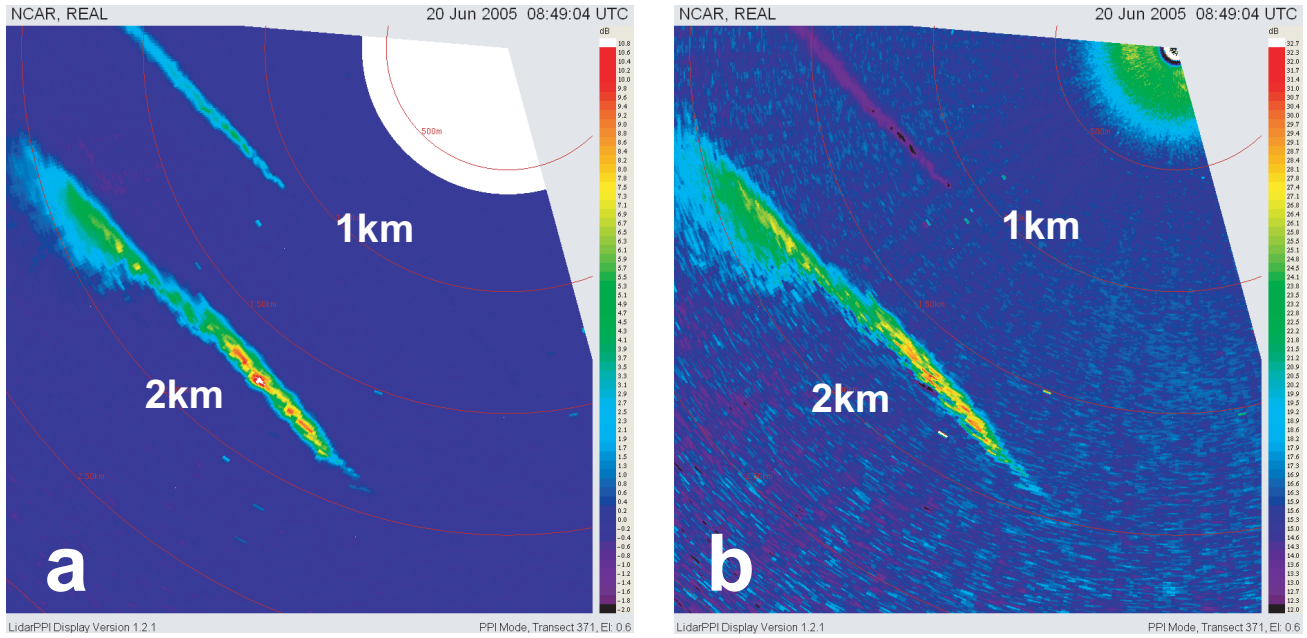


Figure 9. (a) Total backscatter intensity (b) Depolarization ratio. 20 June 2005, 8:49 UTC (2:49 LT). The plume that begins near 1 km range is from a point release of male-specific bacteriophage type 2 (MS2, a bacteriophage representative of viral agents) and the plume near 2 km is from an aerial release of BG. The BG resulted in a higher depolarization and the MS2 a lower depolarization than the background aerosol.

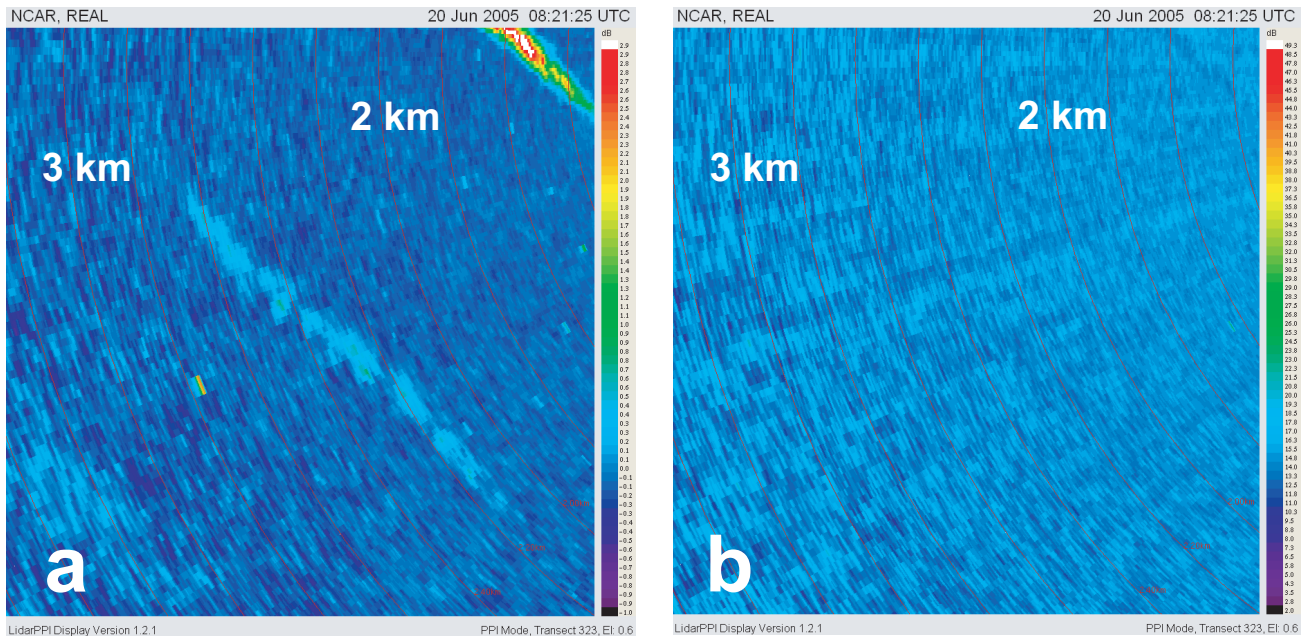


Figure 10. (a) Total backscatter intensity (b) Depolarization ratio. 20 June 2005, 8:21 UTC (2:21 LT). The plume in the middle of the image is a low quantity point release of erwinia herbicola (EH) from 2 km range. The plume in the upper right corner of the images is from a high quantity release of the same material. Although difficult to discern, this aerosol type appears to have a depolarization ratio lower than the background.

plumes were observed in the total backscatter intensity images but without a discernable departure from the depolarization ratio of the background. This may be due to low signal-to-noise caused from low concentration or long ranges, or the plume material possesses similar depolarization to the background aerosol. A more careful analysis of these cases is underway.

Our experience deploying REAL in the field this time revealed some problems and insights on how to remedy them. First, the backscatter data suffer from a small amount of low frequency noise. This is evidenced as radial spokes in the images. We believe this can be reduced by maintaining precise alignment of the optical and mechanical axes of the receiver and beam steering units, respectively. Currently, the beam-steering unit is attached to the roof of the seatainer and the telescope receiver to the interior floor of the seatainer. Precise, constant and repeatable alignment of these two components is difficult—especially in light of the requirement of routine shipping and field environments. A rigid frame that supports the optics table and beam-steering unit would help solve this problem.

Although not shown here, we did notice that the depolarization ratio was elevation angle dependent in some vertical scans. However, for these cases only the data within the first two kilometers of range appeared to be affected. One possible cause of this may be scattering from, or reflection of, the outgoing pulse from the window of the beam steering unit which strikes the photodiode immediately after the laser fires causing a slow recovery of the detector. This problem may be eliminated by tilting the BSU window at a slight angle with respect to the transmit beam. A more careful investigation of this effect will be required to make absolute depolarization measurements in vertical scans.

6. CURRENT AND FUTURE WORK

Increasing the lidar's PRF while maintaining or increasing the pulse energy is highly desirable as it directly increases the angular resolution of the scans and/or increases the temporal resolution (i.e. faster scan update rates), both of which are critical for detection and tracking of plumes. Toward this, we recently purchased a new Nd:YAG pump laser capable of 50 Hz operation at 1.2 J/pulse (Continuum Powerlite 9050). The laser comes with an injection seed for single longitudinal mode operation. We are currently in the process of conducting experiments to determine the performance of the Raman cell at 50 Hz. Unfortunately, fielding the new 50 Hz pump laser will require a new seatainer to accommodate its larger size and heat output and the data acquisition software will need significant modification.

In addition to these tests, we are currently planning to upgrade the InGaAs detector/preamp modules (to CMC Electronics Part number 264-339730-501). These devices offer lower noise than those currently used in a similar package except for a different pin arrangement. We are striving to implement full electronic gain control of the new modules consisting of pre and post amplifiers. This will eliminate the need for the manually operated neutral density filter wheel.

NCAR's Research Applications Laboratory recently began developing algorithms to automatically detect aerosol plumes in the images that REAL provides. We also plan to develop software to extract the vector wind field from motion of the coherent structures.¹¹

Presently, ITT Industries is performing on a contract with NCAR for the creation of a second generation REAL that is designed for continuous and unattended operation. Figure 11 is a diagram of what the unit will probably look like when complete. In addition to continuous and unattended operation, design goals of REAL v2 include operation at 20 Hz and full electronic gain control. This development is an important first step toward networks of surveillance lidars for urban areas. The threat of aerosol bioterrorism is an unfortunate reality of the present age. Much can be done now with currently available lidar technology to begin protecting our cities.

ACKNOWLEDGMENTS

The authors would like to thank the National Science Foundation, NCAR's Earth Observing Laboratory, the U. S. Army, and DARPA for their support in the development and testing of REAL. In particular, Mr. Paul Benda of DARPA and Mr. John Strawbridge (Joint Program Manager, Biological Defense) funded the development of REAL v2 and field testing of the depolarization capability, respectively. We also thank the Dugway Proving

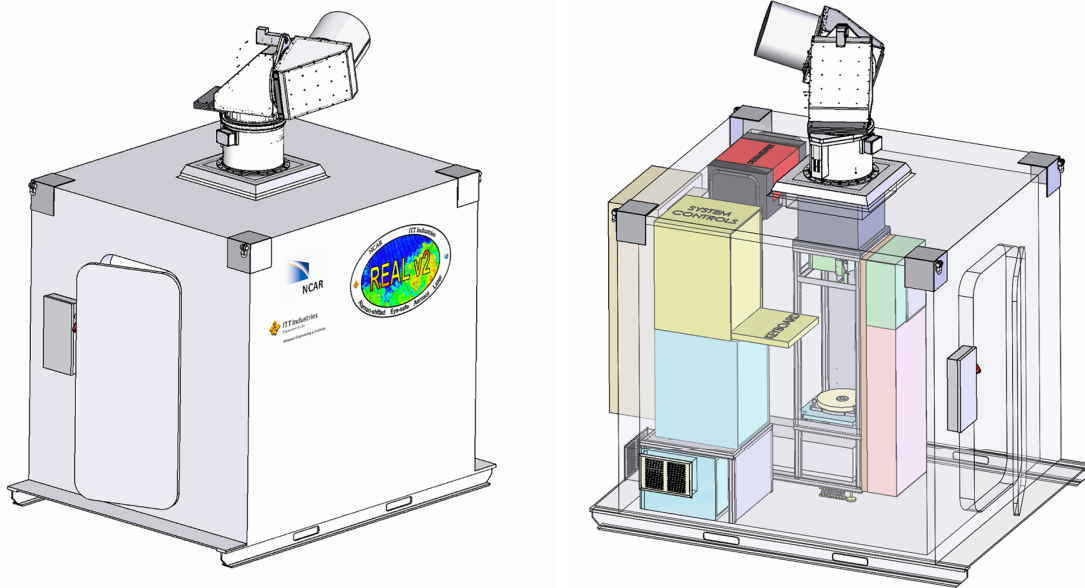


Figure 11. REAL v2 currently being constructed by ITT Industries Advanced Engineering and Sciences Division in Albuquerque, NM.

Ground and Johns Hopkins University Applied Physics Laboratory staff for their outstanding organization and execution of the JBSDS-I2 field experiment. We acknowledge ITT Industries for their achievements during the last year in the design and initial construction of REAL v2. Mr. Tomas Avilez, a summer intern from the University of Arizona, assisted us by creating several of the figures and images in this paper.

REFERENCES

1. A. Fox, "A 21st Century Challenge to Spectroscopists," *Optics and Photonics News* **16**, pp. 26–29, 2005.
2. T. Warner, "The Pentagon Shield Field Program: Toward Critical Infrastructure Protection," *Bull. Amer. Meteor. Soc.*, Submitted in 2005.
3. R. J. Danzig, "Lidar as a Lifeline in Confronting Bioterrorism," *Bull. Amer. Meteor. Soc.* **86**, In Press. To appear in 2005.
4. S. D. Mayor and S. M. Spuler, "Raman-shifted Eye-safe Aerosol Lidar (REAL)," *Appl. Optics* **43**, pp. 3915–3924, 2004.
5. S. M. Spuler and S. D. Mayor, "Scanning eye-safe elastic backscatter lidar at 1.54 microns," *J. Atmos. Ocean. Technol.* **22**, pp. 696–703, 2005.
6. M. S. Webb, P. F. Moulton, J. J. Kasinski, R. I. Burnham, G. Loiacono, and R. Stolzenberger, "High-average-power KTiOAsO₄ optical parametric oscillator," *Opt. Lett.* **23**, pp. 1161–1163, 1998.
7. K. Sassen, "The polarization lidar technique for cloud research: a review and current assessment," *Bull. Amer. Meteor. Soc.* **72**, pp. 1848–1866, 1991.
8. K.-N. Liou and H. Lahore, "Laser sensing of cloud composition: a backscattered depolarization technique," *J. Appl. Meteor.* **13**, pp. 257–263, 1974.
9. K.-N. Liou and R. M. Schotland, "Multiple backscattering and depolarization from water clouds from a pulsed lidar system," *J. Atmos. Sci.* **28**, pp. 772–784, 1971.
10. L. R. Bissonnette, G. Roy, and F. Fabry, "Range-height scans of lidar depolarization for characterizing properties and phase of clouds and precipitation," *J. Atmos. Ocean. Technol.* **18**, pp. 1429–1446, 2001.
11. S. D. Mayor and E. W. Eloranta, "Two-dimensional vector wind fields from volume imaging lidar data," *J. Appl. Meteor.* **40**, pp. 1331–1346, 2001.